Reliable automatic alignment of tomographic projection data by passive auto-focus

A. Kingston,[a] A. Sakellariou, T. Varslot, G. Myers, and A. Sheppard
Department of Applied Mathematics, Research School of Physics and Engineering, The Australian National University, Canberra, ACT 0200, Australia

(Received 7 December 2010; revised 26 May 2011; accepted for publication 16 June 2011; published 9 August 2011)

Purpose: The authors present a robust algorithm that removes the blurring and double-edge artifacts in high-resolution computed tomography (CT) images that are caused by misaligned scanner components. This alleviates the time-consuming process of physically aligning hardware, which is of particular benefit if components are moved or swapped frequently.
Methods: The proposed method uses the experimental data itself for calibration. A parameterized model of the scanner geometry is constructed and the parameters are varied until the sharpest 3D reconstruction is found. The concept is similar to passive auto-focus algorithms of digital optical instruments. The parameters are used to remap the projection data from the *physical* detector to a *virtual* aligned detector. This is followed by a standard reconstruction algorithm, namely the Feldkamp algorithm. Feldkamp *et al.* [J. Opt. Soc. Am. A **1**, 612–619 (1984)].
Results: An example implementation is given for a rabbit liver specimen that was collected with a circular trajectory. The optimal parameters were determined in less computation time than that for a full reconstruction. The example serves to demonstrate that (a) sharpness is an appropriate measure for projection alignment, (b) our parameterization is sufficient to characterize misalignments for cone-beam CT, and (c) the procedure determines parameter values with sufficient precision to remove the associated artifacts.
Conclusions: The algorithm is fully tested and implemented for regular use at The Australian National University micro-CT facility for both circular and helical trajectories. It can in principle be applied to more general imaging geometries and modalities. It is as robust as manual alignment but more precise since we have quantified the effect of misalignment. [DOI: 10.1118/1.3609096]

Key words: tomography, microtomography, geometric calibration, alignment, auto-focus

I. INTRODUCTION

The nondestructive 3D imaging technique known as computed tomography (CT) is used extensively in many fields of research including medicine, biology, geology, and materials science. Three dimensional tomographic images (tomograms) of an object are generated by acquiring many projection images of a static object at different projection angles and then applying a reconstruction algorithm to these images. For high-resolution tomography, where the various system components must be aligned with (sub-) micrometer precision, the projection images do not always adhere to the strict geometrical assumptions of the reconstruction algorithm. The result is that the reconstructed tomograms are totally or partially blurred or *out-of-focus*. Geometric misalignment can be represented by a set of parameters. This paper presents a software method to automate the process of determining (and correcting for) misalignment parameter values, given a model that parameterizes the geometry of the instrument. This removes the associated artifacts from the tomogram.

In essence, we model the geometry of the instrument, parameterizing all the possible misalignments. This is combined with an appropriate fitness function (sharpness) with which to quantify the effects of misalignment on a tomogram. Subject to the value of the parameters, the projection images are remapped from a *physical* detector plane to a *virtual* detector plane. An aligned virtual detector is found when the reconstruction results in the largest sharpness value. The notion of *sharpness* is identical to that defined for passive auto-focus of optical devices. We have been using this alignment method at our micro-CT facility (with circular[1] and helical[2] source trajectories) for over 1 yr and have reconstructed hundreds of tomograms of a range of specimens including: animals, fossils, bones, metals, and rocks. The method has only failed when the sample itself moved substantially during the experiment; for these cases, the proposed method finds the best average alignment.

Combining reference-scan source drift correction (Sasov *et al.*[3]) with the autoalignment method proposed here, the resolution of tomograms at our facility is now principally limited by source spot size. For other systems, typically nano-CT, where mechanical instabilities are an issue, the reprojection method introduced by Mayo *et al.*[4] could be used to refine the time dependant misalignments after the best average misalignment has been found using the proposed method. Alternatively, methods to correct for patient movement could be adapted to apply to source drift in micro-CT. For example, Atkinson *et al.*[5,6] presented a

method in the field of nuclear magnetic resonance imaging that parameterized the trajectory of a patient over the acquisition time in order to find the set of parameter values that minimize the entropy of the reconstruction.

Historically, many techniques have been proposed to solve the problems associated with misaligned tomographic instruments. They fall into three main categories: The first, is to calibrate the instrument by collecting auxiliary data. As a calibration step, or as an experiment prior to the main tomography experiment, projection images of a well defined and specifically designed object are imaged. These images are compared to the expected ideal images and any differences are used to calculate misalignment parameter values.[7–12] The second, is to include fiducial markers in the projection images. These markers are then extracted and tracked to derive the misalignment parameter values.[13] This method is used extensively in electron tomography.[14–16] The third, and far more practical method, is to directly use the tomographic projection images. Various methods have been proposed to date,[17–21] (see Sec. IV for more detail). However, they seem to be either not generally applicable, or lack the robustness and/or precision required to be useful in practice. After applying these methods, manual alignment is typically necessary to correct or refine the misalignment characterization. Thus, manual alignment can be thought of as the most robust software alignment method. We show that a truly reliable automatic method can be formed by emulating this manual alignment (or visual inspection) process.

In this paper, we first define misalignment parameters for cone-beam and parallel-beam x-ray CT in Sec. II. We make use of several simple geometric symmetries to reduce the number of misalignment parameters. We briefly outline methods to correct for known geometric misalignments in Sec. III. Here, we also propose that for the majority of cases software correction of misalignment is indistinguishable from hardware alignment in the resulting tomograms. In Sec. IV, we address the case of unknown misalignment parameter values. Alignment-parameter space is scanned (as detailed in Sec. V) to determine the set of parameter values that yield the sharpest tomogram. To calculate the sharpness of a tomogram for a given set of alignment parameters, all the projection images are mapped from the experimental *physical* detector plane onto a *virtual* detector plane and then a reconstruction is performed. Once the best set of parameters is found, the instrument is virtually aligned and is equivalent to the detector plane being placed at a position which satisfies the strict geometrical requirements of the reconstruction algorithm. Section VI provides an example implementation to demonstrate the success of this method in removing misalignment artifacts from CT reconstructions. This is followed by some concluding remarks in Sec. VII.

II. PARAMETERIZING MISALIGNMENT

Before continuing, it is necessary to define the misalignment of the various components of a CT instrument. Figure 1 depicts the experimental geometry of our circular trajectory cone-beam CT (C-CB-CT) set-up. It contains a source (S), rotation stage (R), and detector (D). For parallel-beam CT (C-PB-CT) the set-up is similar, though the distances $\overline{SR}$ and $\overline{SD}$ are typically not needed for reconstruction; A notable exception is phase-contrast imaging. We have also implemented the technique on a helical trajectory cone-beam CT (H-CB-CT) (Ref. 3) (using FDK reconstruction) which has an additional vertical translation stage (T) located at R.

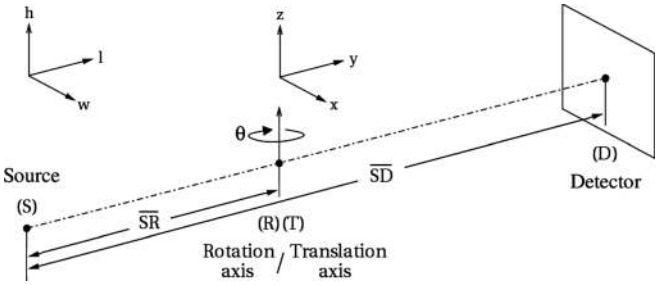

FIG. 1. The geometry of an aligned cone-beam computed tomography instrument. Both circular and helical trajectories are possible.

Let X_η denote the misalignment of component X in direction η, and define ψ, θ, and ϕ as rotations about the w, h, and l-axes, respectively. The three source drift misalignments S_w, S_h, and S_l are actually functions of time and can be corrected using methods such as that proposed by Sasov *et al.*;[3] They will be ignored for the remainder of this paper. Assuming sufficient precision of the rotation and translation stages, there are six misalignments of D, namely: D_w, D_h, D_l, D_ϕ, D_θ, and D_ψ, and four misalignments of R: R_w, R_l, R_ϕ, and R_ψ. Some of these are of course degenerate. For example, R_ϕ is equivalent to D_ϕ. Let, M denote magnification defined as $\overline{SD}/\overline{SR}$ and let L denote $\overline{SD}$; a misalignment $R_w = a$ can be decomposed as $D_w = Ma$, $D_\theta = \arctan(Ma/L)$, and $D_l = \sqrt{L^2 + M^2a^2} - L$. Similarly, a misalignment $R_\psi = \alpha$ can be decomposed as $D_h = L\tan\alpha$, $D_\psi = \alpha$, and $D_l = L(\mathrm{cosec}\alpha - 1)$.

C-PB-CT requires only three parameters to define misalignment: R_w (equivalent to D_w), R_ϕ (equivalent to D_ϕ), and R_ψ. D_l, D_h, and R_l are all unnecessary and D_θ and D_ψ give scaling effects that do not cause inconsistent projections. C-CB-CT requires six parameters, e.g., the full set of detector misalignments. R_l is ignored as it affects only magnification and, for sufficiently large $\overline{SD}$, alignment is not sensitive to detector tilts D_θ and D_ψ. This is supported by the optimal units described below and implies that the detector can be aligned with the spherical wavefront emanating from the x-ray source to sufficient accuracy by eye. Therefore, in practice we use a reduced set of four parameters: R_w, R_ϕ, R_ψ, and D_l. Finally, H-CB-CT requires nine parameters, e.g., all six detector misalignments plus R_l, T_ϕ, and T_ψ. For our set-up this can be reduced to seven, since T is aligned with R to sufficient precision. Detector tilts can not be ignored in this case due to the very high cone-angles utilized.

Throughout this paper, misalignments are measured in *optimal units*. These optimal units essentially normalize the sensitivity to errors in the alignment parameters and provide a stopping criterion when searching for the optimal set of parameters. For any one of the parameters, one optimal unit (ou) is defined as the perturbation in the parameter value required

to approximately cause a maximum one-voxel deviation of any back-projected ray through the tomogram. In accordance with Sakellariou,[22] all parameter values must be determined to a precision of < 0.5 ou to ensure a sharp tomogram.

Given a detector with physical width and height of P_w and P_h mm, respectively, that has $N_w \times N_h$ pixels placed a distance of L mm from the source, the optimal units for the six detector and three rotation stage misalignments are as follows:

D trans. misalignment	Optimal unit (mm)	D rot. misalignment	Optimal unit (rad)	R misalignment	Optimal unit (mm/rad)
D_w	$\frac{P_w}{N_w}\left(\frac{2L}{2L+P_w}\right)$	D_ϕ	$\frac{2}{N_w}\left(\frac{2L}{2L+P_w}\right)$	R_w	$\frac{P_w}{N_w}\left(\frac{2L}{2L+P_w}\right)$
D_h	$\frac{2L}{N_w}$	D_θ	$\frac{4L}{N_w P_w}$	R_ϕ	$\frac{2}{N_w}\left(\frac{2L}{2L+P_w}\right)$
D_l	$\frac{4L^2}{N_w P_w}$	D_ψ	$\frac{8L^2}{N_w P_h^2}$	R_ψ	$\frac{2}{N_w}$

The derivation of these values is given in Appendix A. Note that the magnitude of the optimal units indicates the insensitivity of each parameter to misalignment.

III. CORRECTING FOR KNOWN MISALIGNMENTS

This section describes how corrections are performed once misalignment parameter values are known (either from direct measurement or determined by some software alignment method). There are essentially two correction methods: The first, remaps all the projection images from the experimental *physical* detector plane onto a *virtual* detector plane and then a reconstruction is performed. The second, is to alter the back-projection geometry to account for the misalignments. In practice, we utilize a combination of both. When implementing remapping, 2D Akima interpolation[23,24] is well suited as it is of high accuracy while preserving monotone behavior near sharp boundaries. When computational efficiency is of greater concern than accuracy, "revitalized linear interpolation"[25] may be used. Using this remapping method, followed by Feldkamp–Davis–Kress (FDK) (Ref. 26) reconstruction of the resulting correctly aligned virtual data, we are able to reconstruct accurate tomograms from misaligned data, provided we have knowledge of the misalignment parameters. In Sec. IV, we discuss how to determine these parameters.

For H-CB-CT, provided the Tam–Danielson window remains in the field-of-view, all the data required for an exact reconstruction is present no matter how misaligned. So the difference between alignment by software and hardware is imperceptible. Aligned C-CB-CT has a shadow region of unknown data along the z-axis of the 3D Radon transform (RT). Misalignment of D_h (or R_ψ in the reduced set of parameters) does slightly increase the volume of this unknown region. However, for any reasonable misalignment (i.e., a fraction of the detector height for D_h) this is negligible. We can conclude that alignment by software and hardware is indistinguishable for this case as well. C-PB-CT is unique in this aspect. Unlike CB-CT it has no shadow region when perfectly aligned, however, when misaligned in R_ψ an unknown volume of $0.125\pi N^3 \tan^3 R_\psi$ appears in the 3D-RT. Although, using software correction to correct for an R_ψ misalignment does improve the tomogram (and should always be used to refine the reconstruction quality), hardware alignment is better for this parameter. This is not true for R_w and R_ϕ, which can be aligned equally well with software and hardware.

IV. CORRECTING FOR UNKNOWN MISALIGNMENTS

Since software alignment is indistinguishable from hardware alignment, a reliable postacquisition software correction is preferable as it obviates the need to physically align each experiment, (or to image calibration phantoms), saving a lot of valuable experiment time. There are several proposed methods to align projection data solely based on the data itself. Viskoe[17] presents two methods to correct for R_w only. The first iterative method, minimizes artifacts in the *air* surrounding the object. The second method, estimates R_w as the average center-of-mass of the projection data. Brunetti and DeCarlo[18] also present an iterative method to correct for R_w that minimizes support; *i.e.*, the smallest possible object is the least blurred one. Panetta *et al.*[19] present an iterative method to correct for both R_w and R_ϕ. They discuss how it is also possible (but difficult) to correct for detector tilts. Their method minimizes the difference between data acquired from projection along lines 180° apart in regions of interest (where data approximates a fan beam). Patel *et al.*[20] present a similar method to estimate the axis translation and in-plane rotation by minimizing the difference between 180° projection image pairs. Kyriakou *et al.*[21] model the source trajectory as a circle in an arbitrary plane in order to correct for R_w, R_ϕ, and R_ψ. They iteratively reconstruct the central horizontal slice of the tomogram and aim to minimize entropy.

The most robust method (although not necessarily the most precise) is manual alignment. The manual alignment process scans misalignment parameters through a range of values. This involves reconstructing a selection of one or more 2D slices of the 3D tomogram for the range of assumed misalignments and selecting the image, which looks the best. The alignment-parameter space is scanned to determine the set of parameter values that yield the sharpest tomogram. Once found, the instrument is virtually aligned and is equivalent to the detector plane being placed at a position which satisfies the strict geometrical requirements of the reconstruction algorithm. The visual inspection, i.e., selecting the sharpest reconstructed slice, is the only truly manual part of the process. For a reliable auto-alignment method, we seek to define a fitness function that simulates this visual inspection. The ideal fitness function has several features: (1) it has a global maximum corresponding to an aligned tomogram; (2) it is relatively free of local maxima; and (3) it can be reliably evaluated using only a sub-volume of the complete reconstruction, to save on computation time. The images corresponding to a parameter scan demonstrate a sequence of blurry to sharp, back to blurry behavior analogous to that observed when focusing optical instruments. Figure 2 demonstrates this for the parameters R_ϕ and R_ψ using the liver projection data described in Sec. VI. This behavior suggests that tomogram sharpness is a natural fitness function, since any misalignment of projection data causes blurred tomograms. Given a set of misalignment parameter values, the

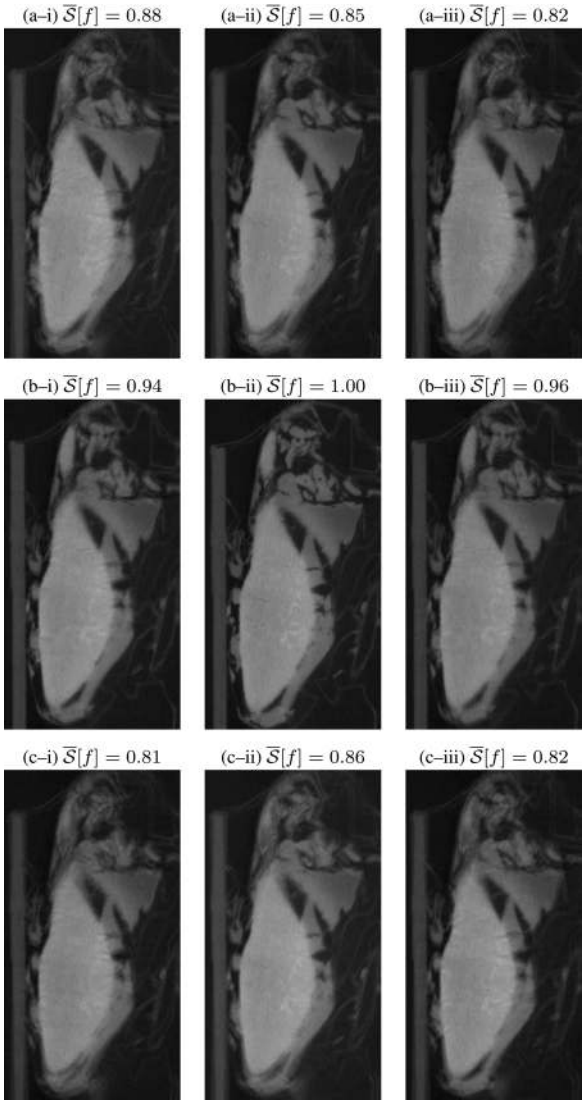

FIG. 2. Depiction of the change in quality and sharpness of a 2D cross-section from a 3D tomogram reconstructed assuming various R_φ and R_ψ misalignments. The cross-section is taken perpendicular to the rotation plane. For rows (a), (b), and (c): $R_\varphi = -4.8$, 1.2, and 7.2 ou, respectively; For columns (i), (ii), and (iii): $R_\psi = -7.5$, 4.5, and 16.5 ou, respectively. The central image coincides with the maximum sharpness for this dataset with $\mathbf{A}^\star = \{-8.76, 1.17, 4.69, -0.84\}$ ou. Sharpness values are calculated according to, and have been normalized by the maximum.

measured projection data can be remapped as described in Sec. III to compensate for these misalignments. We use the set of parameter values that modify the projection data to produce the least blurred, or sharpest, tomogram to quantify the misalignment of the system. We can now formulate automatic misalignment correction as an optimization problem. We seek the parameter set $\mathbf{A} = \{R_w, R_\phi, R_\psi, D_l\}$ that, when used for remapping and reconstruction (as outlined above), produce a tomogram that maximizes sharpness.

Digital optical instruments are commonly focused using passive auto-focus techniques that maximize the image sharpness. This is measured using a "focus function". One of the earliest methods was proposed by Horn in 1968,[27] and new methods continue to be developed and explored as new image processing theory and hardware become available (e.g., Kautsky *et al.*[28]). There have been many comparison studies performed over the years.[29–33]

Sharp images tend to contain the maximum amount of high-frequency information. The act of defocusing, or blurring, suppresses these high frequencies. Therefore, the principle behind most focus functions is to first emphasize the high-frequency information and then quantify it. Methods based on this principle are commonly found to be the most robust, accurate, and unimodal, (i.e., produce a single maximum). These methods include image contrast, image differentiation, and those utilizing the discrete Fourier transform, discrete cosine transform, or wavelet transform. Several other measures have been proposed that do not utilize high-pass filtering. For example, Schlag *et al.*[30] studied image entropy as a candidate. They found that entropy worked well as a measure for a simple edge image, however, the properties completely inverted for a complicated texture image. Our studies with entropy as a focus function for tomographic alignment method agreed. Entropy is based solely on the histogram of an image. It ignores spatial information and does not really indicate sharpness but rather *segmentability*.

IV.A. Fitness function: sharpness

Among the survey literature, it is generally found that the difference in behavior between these various high-pass focus functions is not considerable. This was observed at our facility for C-CB-CT (using FDK reconstruction) when imaging biological, industrial, fossil, and geological tomographic data. The result of this empirical analysis is that an ideal focus function to use is the simplest and fastest: the L_2 norm of image gradient, $||\nabla f||_2$, i.e.,

$$\mathcal{S}[f] = \sum_x \sum_y |\nabla f(x,y)|^2. \tag{1}$$

Here, $|\nabla f|^2$ can be found using the finite difference approximation as $(g * f)^2 + (g^T * f)^2$ where $*$ denotes convolution and g is a localized horizontal gradient convolution kernel such as the Sobel mask:

$$g = \begin{pmatrix} -1 & 0 & 1 \\ -2 & 0 & 2 \\ -1 & 0 & 1 \end{pmatrix}. \tag{2}$$

Alternatively, ∇f can be evaluated using the differentiation property of the Fourier transform. Define the 1D discrete Fourier transform (DFT) of $f(x)$, $x \in [0, N)$, as follows:

$$\mathcal{F}_1[f](u) = \hat{f}(u) = \sum_{x=0}^{N-1} f(x) e^{-i2\pi ux/N}, \quad u \in [0, N), \tag{3}$$

with the inverse DFT being:

$$\mathcal{F}_1^{-1}[\hat{f}](x) = f(x) = \frac{1}{N} \sum_{u=0}^{N-1} \hat{f}(u) e^{i2\pi xu/N}, \quad x \in [0, N). \tag{4}$$

The 2D DFT, ($\mathcal{F}_2$), that maps $f(x,y)$ to $\hat{f}(u,v)$, can be computed as a sequence of 1D DFTs along each dimension. Differentiation in the frequency domain becomes:

$$\frac{\mathrm{d}}{\mathrm{d}x} f(x) = \mathcal{F}_1^{-1}\left[(i2\pi u/N)\hat{f}(u)\right](x), \quad u \in [-N/2, N/2). \tag{5}$$

Since sharpness requires only the L_2 norm of ∇f, it can be found as a ramp filtered image:

$$\mathcal{S}[f] = \sum_x \sum_y \left| \mathcal{F}_2^{-1}\left[(2\pi\sqrt{u^2+v^2}/N)\mathcal{F}_2[f] \right](x,y) \right|^2, \quad \times u,v \in [-N/2, N/2). \tag{6}$$

For FBP type reconstruction this ramp filtering technique is a more efficient and convenient method to calculate sharpness since ramp filtering is already performed as a part of reconstruction. Consider a 2D image f to be reconstructed from a set of 1D projections p_θ for $\theta \in [0, 2\pi)$, with elements, $p_\theta(w)$ for $w \in [0, N)$. Prior to back-projection, the filtering step is performed on the projections to yield:

$$\tilde{p}_\theta = \mathcal{F}_1^{-1}\left[(2\pi\sqrt{u^2}/N)\mathcal{F}_1[p_\theta] \right], \quad \theta \in [0, 2\pi), \tag{7}$$

where $\tilde{p}_\theta$ is the filtered projection. Owing to the Fourier slice theorem, the 2D ramp filtering of f discussed above can be applied simultaneously with this filtering as follows:

$$\bar{p}_\theta = \mathcal{F}_1^{-1}\left[(4\pi^2 u^2/N^2)\mathcal{F}_1[p_\theta] \right], \quad \theta \in [0, 2\pi). \tag{8}$$

Back-projection of these modified projections will yield the ramp filtered image required for sharpness in (6). The L_2 norm computed directly on this image will give $\mathcal{S}[f]$. This method was used to calculate the sharpness of the reconstructed images in Fig. 2 to indicate that sharpness is an appropriate fitness function.

The sharpness measure (2) is strictly not scale invariant; sharpness increases with magnification, $M = \overline{SD}/\overline{SR}$. In order to eliminate magnification during the alignment search, it is assumed that $\overline{SR} = \overline{SD}$; This can be done without loss of generality and voxel dimensions of the tomogram are equivalent to that of the detector pixels. Thus, varying D_l only alters the angle of back-projected rays without magnifying the reconstructed image. (Note that this assumption breaks down for the high cone-angles that can be used in H-CB-CT; a modified solution for scale invariance for this case is presented in Ref. 34). A scan over D_l can be performed to identify an aligned system. After the misalignment parameter values have been determined and a reconstruction from an aligned projection set has been performed, the voxel dimensions are scaled by $1/M$. The uncertainty in the final scale is proportional to that in $\overline{SR}$.

IV.A.1. Simulated D_l misalignment

Figure 3 demonstrates this scale invariance with various values of D_l misalignment. A high-resolution 256×256 mm image of the standard head phantom was projected to 403 equally spaced projections simulating 360-C-CB-CT. A 1D detector with 256 pixels of dimension 2 mm was used with $\overline{SR} = 500$ mm and $\overline{SD} = 1000$ mm. Reconstructions were performed assuming $\overline{SD}$ long by 3.2 ou, i.e., 1098 mm, for values of D_l from -10 ou up to 10 ou in steps of 1 ou $= 30.52$ mm. Note, in the reconstructed images that the phantom does not change size but does cause degradation. Sharpness was evaluated at each instance using (6). A parabolic fit to the sharpness data estimates D_l as approximately -2.8 ou.

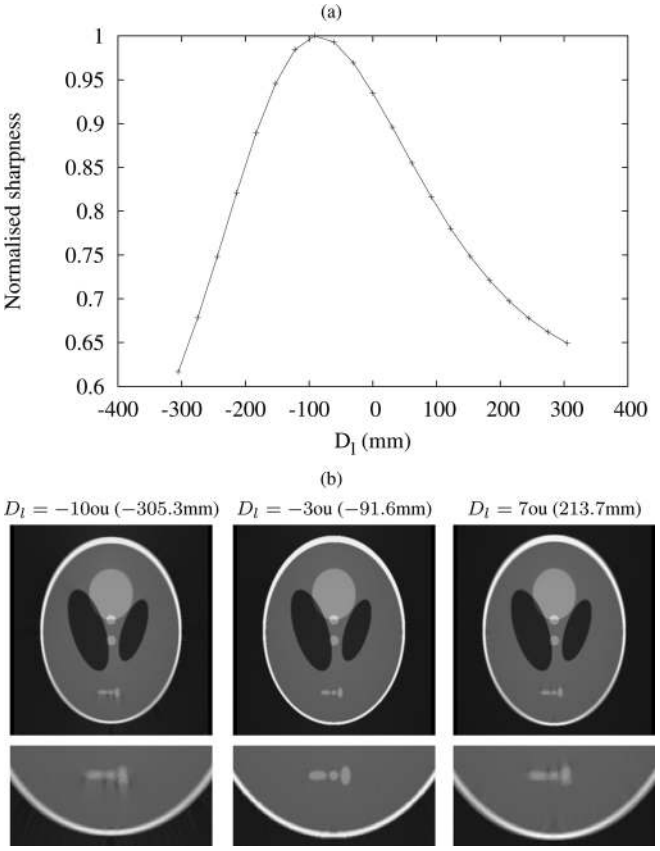

FIG. 3. (a) Normalized sharpness plot obtained from the 1D scan of D_l using an assumed value of $\overline{SD} = 1098$ mm. The true $\overline{SD} = 1000$ mm corresponds to $D_l = -98$ mm or -3.2 ou. Sharpness is determined using (6) via projection filtering described in (8). The peak is located at $D_l = -86$ mm or -2.81 ou. (b) A selection of the images reconstructed, assuming $D_l \in \{-10, -3, 7\}$ ou. The range of the presented images is $[-0.2, 1.2)$, with [0,1) corresponding to the range of the original phantom.

IV.A.2. Simulated R_w misalignment

Figure 4 demonstrates the performance of the sharpness function with various values of R_w misalignment. A high-resolution image of the standard head phantom was projected to 403 equally spaced projections simulating 360-C-PB-CT. Note that $403 = \lceil 256\pi/2 \rceil$ is below the Nyquist frequency but is a sufficient number of projections such that the ramp filter can be used without introducing artifacts in the reconstruction. The projection data was then translated off-center by 5.7 ou (1 ou = 1 pixel) in order to simulate an R_w misalignment. 256×256 tomogram reconstructions were performed assuming values of R_w from -10 ou up to 10 ou in steps of 1 ou. The tomogram pixel dimensions are equivalent to that of the detector elements. Sharpness was evaluated at each instance using (6). Parabolic fits to the sharpness data estimates R_w as approximately -5.9 ou for data with 0 and 10% noise and -5.5 ou for data with one quarter the number of projections. For simplicity, the noise model follows a normal distribution with a standard deviation one tenth that of the projection data.

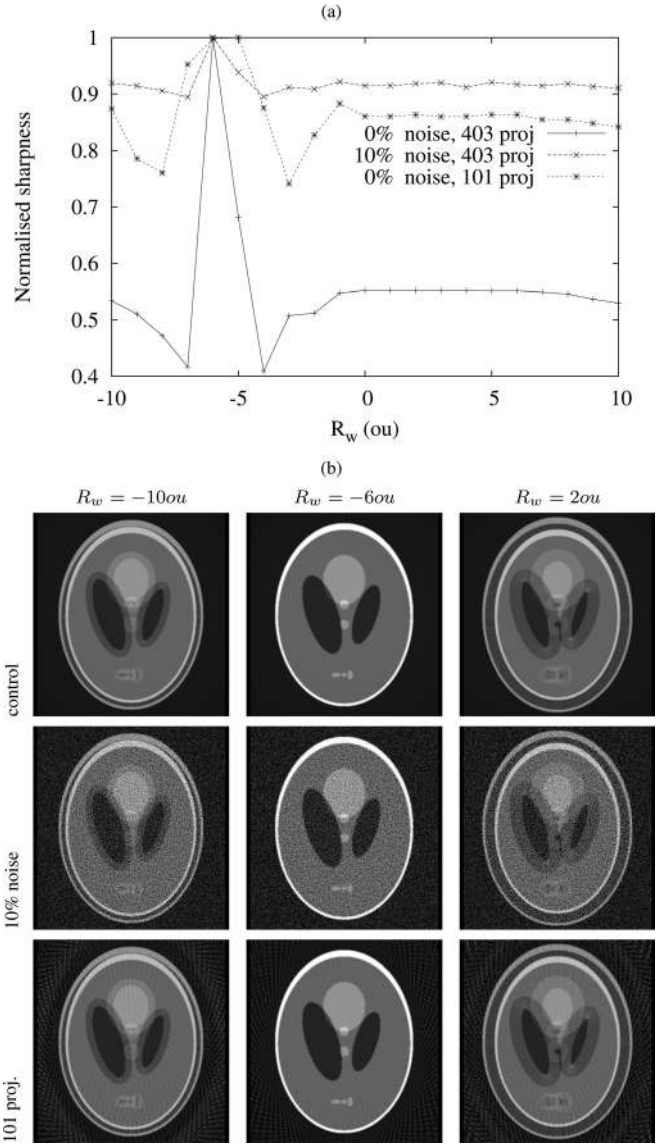

FIG. 4. (a) Sharpness plots obtained from the 1D scans of R_w normalized by maximum sharpness. Sharpness is determined using (6) via projection filtering described in (8). The peak is located at -5.85 and -5.87 ou for data using 403 projections with 0 and 10% noise, respectively, and -5.48 ou for data using 101 noise free projections. (b) A selection of the images reconstructed assuming $R_w \in \{-10, -6, 2\}$ ou. The range of the presented images is $[-0.2,1.2)$, with [0,1) corresponding to the range of the original phantom.

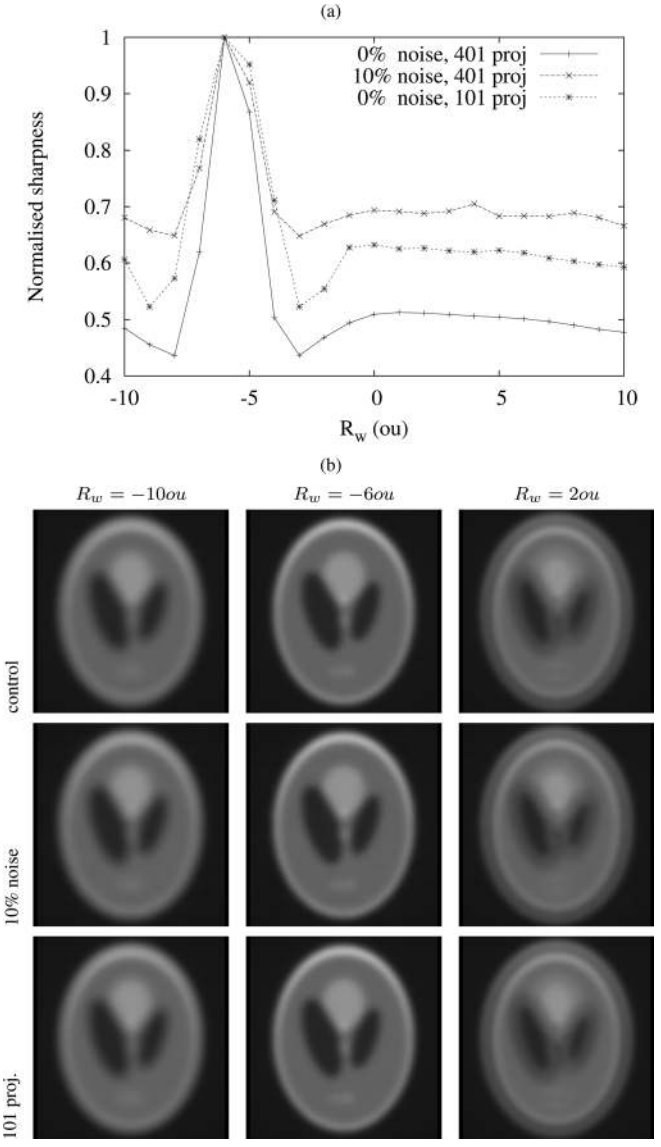

FIG. 5. (a) Sharpness plots obtained from the 1D scans of R_w normalized by maximum sharpness. Sharpness is determined using (9) via projection filtering described in (10) with $\sigma = \pi/4$. The peak is located at -5.75 and -5.75 ou for data using 403 projections with 0 and 10% noise, respectively, and -5.71 ou for data using 101 noise free projections. (b) A selection of smoothed reconstructed images for $R_w \in \{-10, -6, 2\}$ ou. The range of the presented images is $[-0.2,1.2)$, with [0,1) corresponding to the range of the original phantom.

IV.A.3. Robustness of the Sharpness metric

Sharpness as defined above is sensitive to fluctuations not related to image edges, such as image noise and streaking from course angular sampling by projections. This is demonstrated by the reduced peak strength for noisy and undersampled circumstances in Fig. 4. The influence of these effects can be reduced by soft thresholding the image gradient and/or low-pass filtering the data before applying differentiation.[32] Figure 5 demonstrates the performance of the sharpness function when combined with low pass filtering. The head phantom data from Fig. 4 was reevaluated sharpness function when combined using a Gaussian windowed ramp filter in the frequency domain, i.e.,

$$\mathcal{S}[f] = \sum_x \sum_y \left| \mathcal{F}_2^{-1} \left[(2\pi\sqrt{u^2+v^2}/N) e^{-(u^2+v^2)N^2/8\pi^2\sigma^2} \times \mathcal{F}_2[f] \right](x,y) \right|^2, \tag{9}$$

for $u, v \in [-N/2, N/2)$. This was implemented by modifying the filtering in the FBP reconstruction according to the following:

$$\bar{p}_\theta = \mathcal{F}^{-1} \left[(4\pi^2 u^2/N^2) e^{-u^2N^2/8\pi^2\sigma^2} \mathcal{F}[p_\theta] \right], \tag{10}$$

where $\sigma = \pi/4$ and the L_2 norm of the reconstruction gives sharpness. Parabolic fits estimate R_w as -5.75 ou for data with 0 and 10% noise and -5.71 ou for data with one quarter the number of projections.

Given a reconstruction algorithm that assumes a correctly aligned CT imaging system, the above form of sharpness works well for system alignment given source trajectories such as 360-C-{PB,CB}-CT and H-CB-CT. These are smooth trajectories without end-points and misalignment results in blurring. Modalities such as 180-C-{PB,CB}-CT have trajectory specific end-points and, as well as blurring, large streaking artifacts result from misaligned data. Another fitness function (or a modified reconstruction method during the alignment process) may be more appropriate in these cases, however, the principle remains the same.

IV.B. Auto-focus procedure for determining misalignment

Using this focus function, together with the detector remapping technique described above, we are now able to solve for, and correct for, the misalignment parameters in a cone-beam CT system. For a given set of parameters $\mathbf{A}$, we: (1) remap the data; (2) from this remapped data, we reconstruct several slices through the object using (in this case) the FDK algorithm; and (3) evaluate the sharpness of each of these slices, as discussed above. Parameter space is then searched for the set $\mathbf{A}^\star$ that produces the sharpest reconstruction. Finally, the parameter set $\mathbf{A}^\star$ is used to reconstruct a full, correctly aligned tomogram.

The scanning process is outlined in the following section and an example implementation for a C-CB-CT scan is given in Sec. VI. For the H-CB-CT with FDK reconstruction the process is identical but with some additional parameters. Alignment of H-CB-CT with theoretically exact reconstruction methods such as that introduced by Katsevich[35] is more complicated (as it is similar in concept to 180-C-PB-CT). Adaptation of the proposed method for this mode is detailed in Ref. 34.

V. SCANNING MISALIGNMENT PARAMETER SPACE

A four-dimensional, brute-force parameter search is not the most computationally efficient way of finding the correct misalignment parameters. We define here a simple scanning process that takes approximately as much CPU time as the final, full-volume reconstruction, and occurs automatically, i.e., without human input. There are several key components to making the search efficient: (1) reconstruct only 2D slices for inspection, (2) a set of 1D (or 2D) scans only, (3) the parameter search order and/or combinations, and (4) a multiscale search. Pseudocode outlining the procedure is presented in Appendix B.

V.A. 2D slice reconstruction

Note that for each evaluation of a set $\mathbf{A}$ we need only reconstruct a few representative slices through the object, rather than the full 3D volume. This speeds up the search process significantly. The FBP reconstruction of an N^3 tomogram from $O(N)$ projections requires $O(N^4)$ computations. A set of K 2D slices require only $O(KN^3)$ computations. Typically, at our facility $K = 5$ and $N = 2048$ giving a $400\times$ speed up.

V.B. 1D (or 2D) parameter scans

The parameters are not entirely independent; for a given horizontal slice, $z = \eta$, $R_w = \delta$ can be approximately canceled by an axis rotation of $R_\phi = \arctan(-\delta/\eta)$. Similarly, $R_\psi = \delta$ can be approximately canceled by a detector translation of $D_l = 1 - \eta/(L\sin\delta + \eta\cos\delta)$. Therefore, 4D parameter space can be scanned as two separate 2D scans over $\{R_w, R_\phi\}$ and $\{R_\psi, D_l\}$.

Selecting K slices for reconstruction that are distributed, throughout the volume minimizes the correlation of parameter misalignment effects; An example slice selection could be $K = 5$ horizontal slices for $z \in \{-P_h/3, -P_h/6, 0, P_h/6, P_h/3\}$. The scan over 4D parameter space can then be performed as a set of 1D scans over each of the parameters in $\mathbf{A}$.

V.C. Parameter scan order

The determination of optimal units for each misalignment parameter gives a stopping criterion, i.e., when each parameter value is known to within 0.5 ou. The relative magnitude of these optimal units also indicates the sensitivity of each parameter, and hence the parameter scans order. R_w and R_ϕ have the smallest optimal units and so should be determined first followed by R_ψ and then D_l.

V.D. Multiscale approach

FBP reconstruction of K 2D slices of the tomogram from $O(N)$ projections is performed in $O(KN^3)$ computations. Therefore, K 2D slices downsampled to S^2, where $S = N/b$, reconstructed from $O(S)$ projections downsampled to S^2 is performed b^3 times faster. We refer to b as the binning value. Using a binning of 4, the parameter scan can be performed 64 times faster.

Figure 6 demonstrates that up to resolution the location of maximum sharpness is invariant under downsampling. Note that at each resolution, for a binning by b, we step by b optimal units when scanning a parameter. This removes any inconsistencies due to different degrees of interpolation.

The 1D scans over each of the parameters in $\mathbf{A}$ can be performed at multiple resolutions. The initial set of extremely fast coarse-resolution scans with $b = 4$ can be broad to identify approximate parameter values in $\mathbf{A}^\star$. These can then be refined at the subsequent finer resolutions, $b \in \{2, 1\}$ using highly localized searches. A parabolic fit is applied around the peak of each plot to improve the estimate of the parameter values.

V.E. Optimization

The above set of multiscale 1D searches complete the scan of parameter space very quickly. We found no need to implement further optimization techniques such as the golden section search, the simplex method, Powell's method, or gradient based techniques. It should be noted that using a

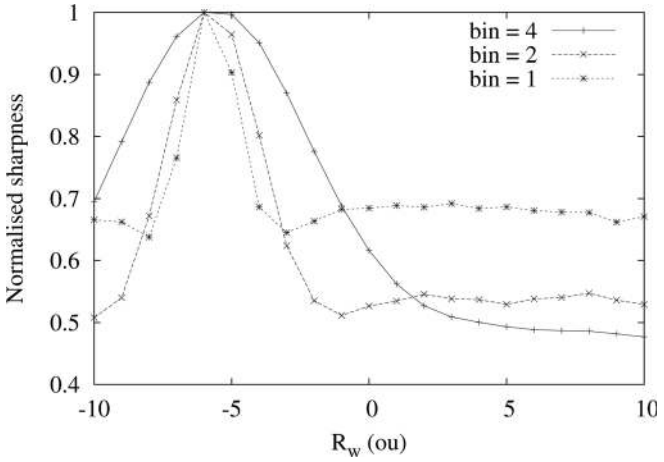

FIG. 6. Sharpness plots obtained from the 1D scans of R_w normalized by maximum sharpness. Sharpness is determined as in Fig. 5 on the projection set with 10% noise. The peak is located at -5.55, -5.72, and -5.85 ou for data with binning of 4, 2, and 1, respectively.

greater degree of blurring in the sharpness calculations causes the fitness function to behave more suitably for such techniques without altering the location of maximum sharpness. This has been demonstrated in Fig. 7 for the head phantom dataset with 10% noise using a Gaussian window (applied to the ramp filter in Fourier space) with various standard deviations, σ.

VI. IMPLEMENTATION AND CASE STUDY—RABBIT LIVER

In what follows, we apply our auto-focus scheme to real data. The example demonstrates that: (1) the auto-focus procedure can determine misalignment parameters with sufficient precision to remove the associated artifacts, using only the original projection data; (2) our chosen parameters are sufficient to characterize misalignments in a circular cone-beam CT system; and (3) the L_2 norm of the image gradient is an appropriate fitness function to measure misalignment.

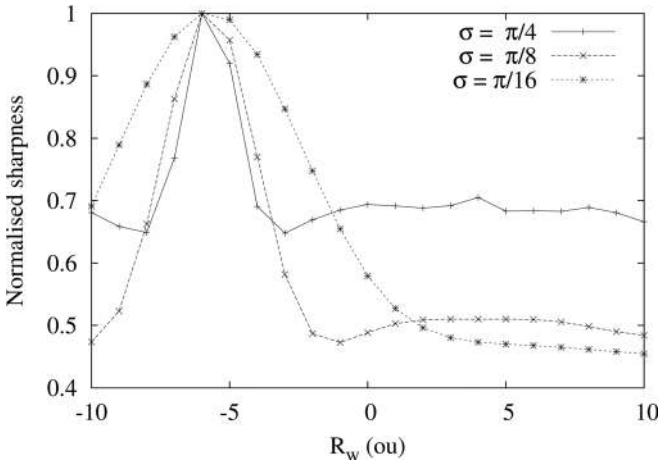

FIG. 7. Sharpness plots obtained from the 1D scans of R_w normalized by maximum sharpness. Sharpness is determined sharpness determined as in Fig. 5 with $\sigma \in \{\pi/4, \pi/8, \pi/16\}$ on the projection set with 10% noise. The peak is located at -5.75, -5.72, and -5.70 ou, respectively.

The case study specimen is a rabbit liver fixed in wax, as shown in Fig. 2. (This image also serves to demonstrate the effect that a perturbation of parameter values R_ϕ and R_ψ have on reconstruction quality and corresponding sharpness). The projection data were collected with $\overline{SD} = 1000$ mm and $\overline{SR} = 600$ mm. The pixel size of the detector was 33.6×33.6 μ m, binned by 2 so that the effective voxel size of the tomogram is approximately 40 μ m. After binning the square detector size is $N = 1024$ pixels and a 1024^3 tomogram is reconstructed from 1440 projections. This experiment was performed in 2007, and is used in this demonstration because it was not physically aligned very well. A demonstration of the improvement in image quality achieved by using the auto-focus software alignment of projection data is presented in Fig. 8.

To demonstrate the efficacy with which the auto-focus technique can correct the misalignment, plots of sharpness values for each of the 12 iterations are shown for experimental data. Sharpness is determined according to (9), by filtering the projection data as in (10) with $\sigma = \pi/4$. It has been averaged over five horizontal slices distributed throughout

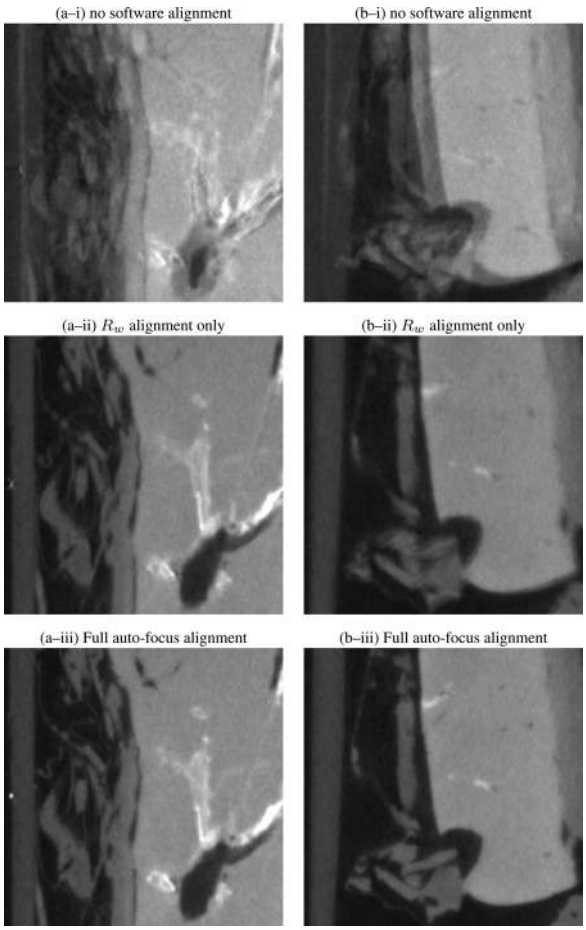

FIG. 8. (a) and (b) each show a selected 256×256 subsection of 2D slices of the reconstructed 1024 tomogram. The following software projection alignment implemented: (i) none ($\mathbf{A}^\star = \{0, 0, 0, 0\}$ ou), (ii) R_w alignment only [as is common in literature], ($\mathbf{A}^\star = \{-8.76, 0, 0, 0\}$ ou), and (iii) alignment by the full set of parameter values specified by the auto-focus procedure, ($\mathbf{A}^\star = \{-8.76, 1.17, 4.69, -0.84\}$ ou). The two slices are perpendicular to the rotation plane.

the tomographic volume. Each plot is normalized by the maximum sharpness of the entire process. Figure 9(a) shows the results of the initial set of four broad coarse-scale parameter scans. After these coarse-scale iterations $\mathbf{A}^\star = \{-10.44, 1.17, 4.55, 0.31\}$ ou. Figure 9(b) shows the results of the next set of four mid-scale parameter scans. Following these mid-scale scans $\mathbf{A}^\star$ is refined to $\{-9.21, 1.08, 4.78, -0.75\}$ ou. Figure 9(c) shows the results of the final set of four full-scale parameter scans. The best and final set of parameter values is $\mathbf{A}^\star = \{-8.77, 1.16, 4.61, -0.84\}$ ou. The entire auto-focus process 1.5 times faster than the final full-scale 3D reconstruction. It can be seen from the final results that all misalignment parameter values were nonzero, however, the auto-focus process quickly located the best values for each parameter. To investigate accuracy, the 1D scan of each parameter was repeated at full resolution to yield $\mathbf{A}^\star = \{-8.76, 1.17, 4.69, -0.84\}$. No parameter value has changed by more than 0.1 ou which is well below the required resolution of 0.5 ou. So the three sets of 1D scans at multiple resolutions is sufficient for convergence.

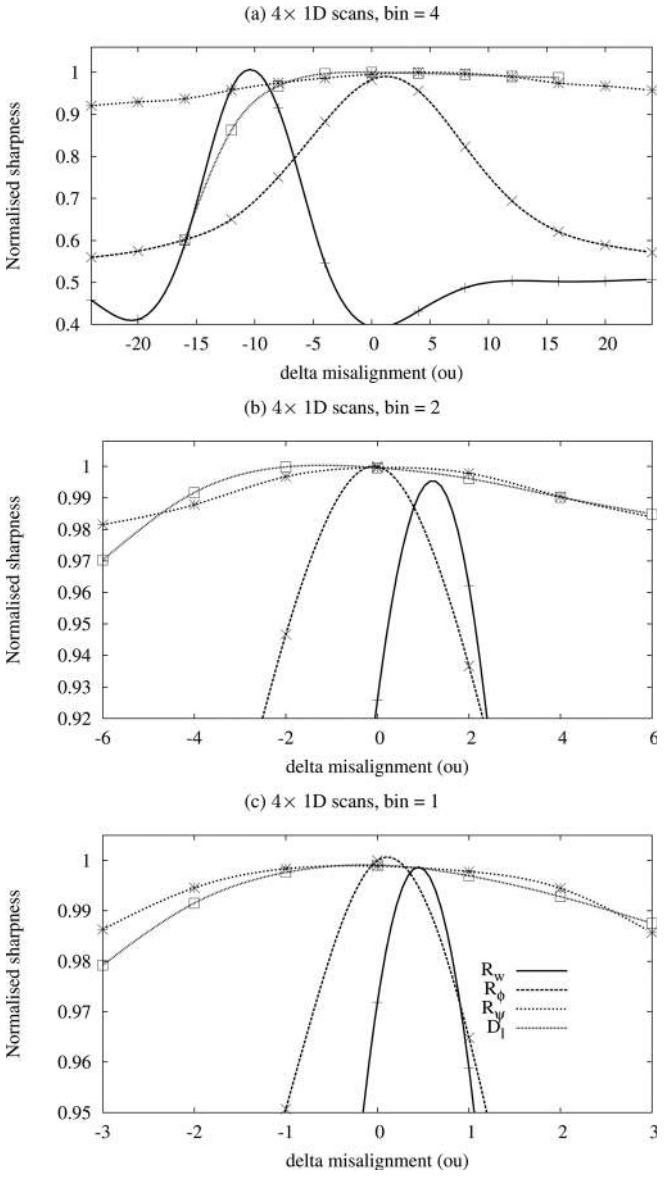

FIG. 9. The sharpness *profiles* obtained from the 1D scans of parameters R_w, R_φ, R_ψ, and D_l at various resolutions as described in Sec. VI: (a) coarse resolution (bin = 4), (b) mid resolution (bin = 2), and (c) full resolution (bin = 1). The ordinate is the change in misalignment from the assumed values of $\mathbf{A}^\star$. The system is initially assumed to be aligned, *i.e.*, $\mathbf{A}^\star = \{0, 0, 0, 0\}$ in plot (a), then accepts the values identified in the 1D scans in (a) to become $\mathbf{A}^\star = \{-10.44, 1.17, 4.55, 0.31\}$ for plot (b) and likewise $\mathbf{A}^\star = \{-9.21, 1.08, 4.78, -0.75\}$ for plot (c). Note, the key in plot (c) applies to all plots.

VII. CONCLUSION

A robust and precise method to automate alignment of tomographic projection data using passive auto-focus has been presented. This procedure can be applied to any tomography data, even retrospectively on archived data previously thought unusable, without any additional information. Our auto-focus alignment method works for FDK reconstruction from circular and helical source trajectories, but should work for any reconstruction algorithm that assumes a correctly aligned CT imaging system. The process reliably aligns to sub-pixel accuracy and, since the experimental data itself is used for calibration, it automatically aligns to the precision required regardless of scale. If all component movement, such as source drift and rotation stage eccentricity are ignored, this method will find the sharpest *time-averaged* tomogram. However, we have verified that this method can be extended to correct for such problems; all that is required are appropriate parametrized models.

ACKNOWLEDGMENTS

The authors acknowledge the member companies of the Digital Core Consortium for providing funding support and the Australian Partnership for Advanced Computation for supplying computing resources. Thanks to Dr. Shane Latham for helpful discussions on optimization techniques and Dr. Tim Senden for providing the experimental data.

APPENDIX A: OPTIMAL UNIT DERIVATIONS

Here, we establish the perturbation required for each misalignment parameter that approximately produces at most a 1 voxel deviation of backprojected rays from their true trajectory throughout the $N_w \times N_w \times N_h$ reconstruction volume. We denote these perturbations *optimal units* (ou). Approximate ou values are derived here assuming a $Nw \times Nh$ pixel detector with physical dimensions P_w mm $\times$ P_h mm placed at $L = \overline{SD}$ mm with a specimen placed at $\overline{SR}$ mm. Throughout the following, we assume that $P_w \geq P_h$, $Nw \geq N_h \gg 2$ and that detector pixels are square, i.e., $P_w/N_w = P_h/N_h$.

1. OPTIMAL UNITS FOR MISALIGNMENTS IN D

There are six detector misalignments, three translations and three rotations as described in Sec. II. Since uncertainty in $\overline{SR}$, i.e., $|R_l| > 0.0$ mm, does not cause misalignment, when performing reconstruction by backprojection it is convenient to assume the detector lies at the center of the specimen, i.e., $\overline{SR} = L$. This eliminates magnification as a contributing factor to sharpness and gives reconstructed

voxel dimensions identical to that of the detector pixels, i.e., P_w/N_w mm. Then misalignment in the reconstruction is proportional to misalignment in the detector. In this context, $L = P_w/2$ corresponds to the source rotating at the boundary of the reconstructed volume and serves as a reasonable lower limit for L. After reconstruction, voxel dimensions are scaled by $\overline{SR}/L$.

a. An optimal unit in D_w

Due to the cone angle geometry, we require the horizontal shift at the detector that corresponds to a 1 voxel shift (P_w/N_w mm) at the far side of the reconstructed volume, i.e., $L + 0.5P_w$. This has been depicted in Fig. 10(a). This corresponds to $\delta_w = \frac{P_w}{N_w}\left(\frac{2L}{2L+P_w}\right)$.

b. An optimal unit in D_h

Consider the ray backprojected through the center of the central horizontal slice, $z = 0$. We require the change in detector height of δ_h that translates the point of back-projection at the far side of the reconstructed volume by 1 voxel, (or P_w/N_w mm), as depicted in Fig. 10(b). This corresponds to $\delta_h = 2L/N_w$.

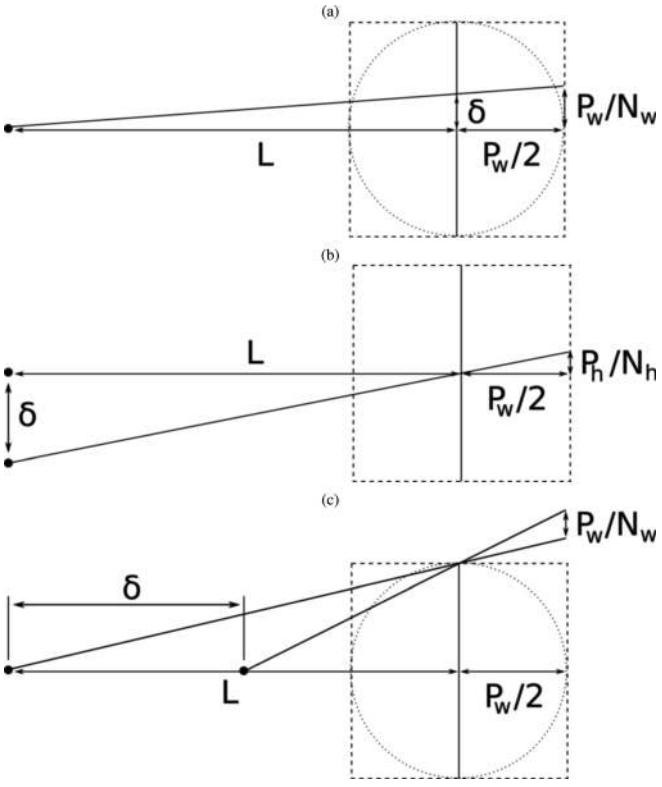

FIG. 10. (a) A translation by 1 voxel (or P_w/N_w mm) at the far side of the reconstructed volume corresponds to $\delta_w = 1$ ou at the detector. (b) A change in backprojection angle causing a translation by 1 voxel (P_h/N_h) at the far side of the reconstructed volume corresponds to $\delta_h = 1$ ou of the detector. (c) A change in backprojection angle causing a translation by 1 voxel (P_w/N_w) at the far side of the reconstructed volume corresponds to $\delta_l = 1$ ou of the detector.

c. An optimal unit in D_l

Consider, the ray backprojected through the center of the vertical slice at $x = 0.5P_w$. We require the change in detector length of δ_l that translates the point of back-projection at the far side of the reconstructed volume by 1 voxel (or $P_h/N_h = P_w/N_w$ mm), as depicted in Fig. 10(c). Similar triangles give $x = P_h(L + 0.5P_w)/2L$ and we require

$$x + \frac{P_w}{N_w} = (L - \delta_l + 0.5P_w)\frac{P_h}{2(L-\delta_l)}. \tag{A1}$$

Substituting in the above equation for x and assuming $N_w \gg 2$, this simplifies to give $\delta_l = 4L^2/(N_w P_w)$.

d. An optimal unit in D_ϕ

An optimal unit for in-plane rotation can be found as that which gives a 1 ou translation, δ_w, calculated above at a radius of $0.5P_w$, i.e., $\delta_\phi = \arctan(2\delta_w/N_w)$. Assuming $P_w \geq P_h$ and $N_w \gg 2$, this simplifies to the following $\delta_\phi \simeq \frac{2}{N_w}\left(\frac{2L}{2L+P_w}\right)$.

e. An optimal unit in D_θ

Observe the geometry in Fig. 11(a). This depicts a θ rotation of the detector that causes the backprojected ray passing through the edge pixel of the detector to shift by 1 pixel in the corrected *virtual detector*. Through the sine rule we find horizontal component of δ_θ^h as follows:

$$\delta_\theta^h = \arcsin\left(\frac{2x\cos\alpha'}{P_w}\right) \simeq \frac{2x\cos\alpha'}{P_w}. \tag{A2}$$

The cosine rule can be used to obtain the following relationship in order to find x:

$$0.25P_w^2 = x^2 + (0.5P_w - P_w/N_w)^2 - 2x(0.5P_w - P_w/N_w)(\cos\alpha\prime + 0.5\pi). \tag{A3}$$

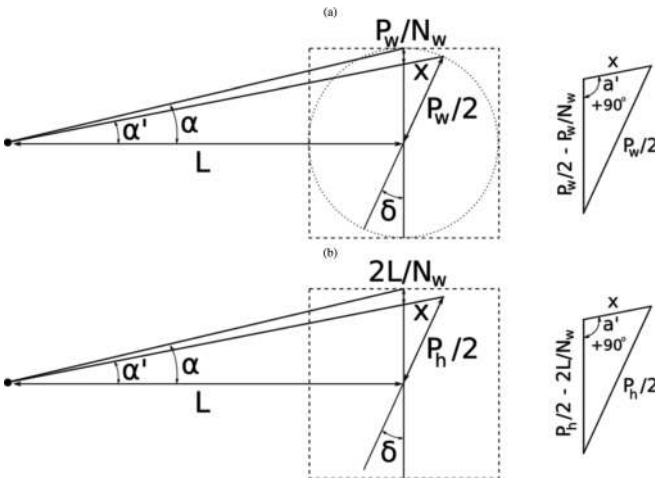

FIG. 11. (a) A change in detector angle causing a translation by 1 voxel (P_w/N_w) at the edge of the reconstructed volume corresponds to $\delta_\theta^h = 1$ ou of the detector. (b) A change in detector angle causing a translation by $\delta_h = 2L/N_w$ at the edge of the reconstructed volume corresponds to $\delta_\psi^v = 1$ ou of the detector.

Noting that $\sin\theta = -\cos(\theta + 0.5\pi)$ and that the x^2 term can be ignored we obtain the following:

$$x = \frac{P_w^2/N_w - P_w^2/N_w^2}{(0.5P_w - P_w/N_w)\sin\alpha\prime}. \quad \text{(A4)}$$

Note that the term P_w^2/N_w^2 can be ignored. By substituting this expression back into the equation for δ_θ^h and observing that $\tan\alpha\prime = L/(0.5P_w - P_w/N_w)$, we obtain $\delta_\theta^h \simeq 4L/(N_w P_w)$.

The vertical component δ_θ^v can be found using the value of δ_l. A rotation of the detector by δ_θ^v causes a change in L at the edge of the detector by $0.5P_w \tan\delta_\theta^v \simeq 0.5P_w\delta_\theta^v$. If we set this equal to the value of δ_l obtained above, we see that $\delta_\theta^v \simeq 8L^2/(N_w P_w^2) = 2L\delta_\theta^h/P_w$. Assuming $L \geq 0.5P_w$, δ_θ^h is always smaller than δ_θ^v and so δ_θ^h is used to define an optimal unit in D_θ.

f. An optimal unit in D_ψ

Observe the geometry in Fig. 11(b). This depicts a ψ rotation of the detector that causes the backprojected ray passing through the edge pixel of the detector to shift by $\delta_h = 2L/N_w$ in the corrected *virtual detector*. Through the sine rule we find vertical component of δ_ψ^v as follows:

$$\delta_\psi^v = \arcsin\left(\frac{2x\cos\alpha\prime}{P_h}\right) \simeq \frac{2x\cos\alpha\prime}{P_h}. \quad \text{(A5)}$$

The cosine rule can be used to obtain the following relationship in order to find x:

$$0.25P_h^2 = x^2 + (0.5P_h - 2L/N_w)^2 - 2x(0.5P_h - 2L/N_w)(\cos\alpha\prime + 0.5\pi). \quad \text{(A6)}$$

Noting that $\sin\theta = -\cos(\theta + 0.5\pi)$ and that the x^2 term can be ignored we obtain the following:

$$x = \frac{L(P_h - 2L/N_w)}{N_w(0.5P_h - 2L/N_w)\sin\alpha\prime}. \quad \text{(A7)}$$

Ignoring the term $2L/N_w$ in the numerator, substituting this expression back into the equation for δ_ψ^v, and observing that $\tan\alpha\prime = L/(0.5P_h - 2L/N_w)$, we obtain $\delta_\psi^v \simeq 8L^2/(N_w P_h^2)$.

The horizontal component δ_ψ^h can be found using the value of δ_l. A rotation of the detector by δ_ψ^h causes a change in L at the edge of the detector by $0.5P_h \tan\delta_\psi^h \simeq 0.5P_h\delta_\psi^h$. If we set this equal to the value of δ_l obtained above, we see that $\delta_\psi^h \simeq 8L^2/(N_w P_w P_h) = P_w\delta_\psi^v/P_h$. Therefore, δ_ψ^v is always less than or equal to δ_ψ^h and so δ_ψ^v can be used to define an optimal unit in D_ψ.

2. OPTIMAL UNITS FOR MISALIGNMENTS IN R

There are three rotation stage misalignments one translation and two rotations as described in Sec. II. An optimal unit for these parameters can be derived from those for D, e.g., it has been established that $R_\phi = D_\phi$.

a. An optimal unit in R_w

A misalignment $R_w = a$ mm can be decomposed as $D_w = Ma$ mm, $D_\theta = \arctan(Ma/L)$ rad, and $D_l = \sqrt{L^2 + M^2a^2} - L$ mm where $M = L/\overline{SR}$. By setting D_w, D_θ, and D_l to 1 ou (as defined above) and solving for a, we find R_w as the minimum of these which corresponds to the D_w term. Therefore, 1 ou in R_w is $\frac{P_w}{MN_w}\left(\frac{2L}{2L+P_w}\right)$ mm.

b. An optimal unit in R_ψ

A misalignment $R_\psi = \alpha$ rad can be decomposed as $D_h = L\tan\alpha$ mm, $D_\psi = \alpha$ rad, and $D_l = L(\text{cosec}\alpha - 1)$ mm. By setting D_h, D_ψ, and D_l to 1 ou (as defined above) and solving for α, we find R_ψ as the minimum of these, which corresponds to the D_h term. Therefore, 1 ou in R_ψ is $2/N_w$ rad.

APPENDIX B. PSEUDOCODE TO SCAN PARAMETER SPACE

The pseudocode below scans 1 parameter at a time. The search range for a parameter with current estimate Xou is denoted by $A:B$ and defined as $[X-A, X+B]$ with sharpness evaluated at $\{X-A, X-A+\text{BIN}, X-A+2\text{BIN}, \ldots, X+B\}$. Sharpness is averaged over K reconstructed slices. The search ranges $A:B$ and the K specified slices for each parameter and resolution should be tailored to the specific system. At the coarsest resolution scans are very fast and can be quite broad; for example at our facility, with $N = 2048$, the initial search for R_w is $A:B = -128$ ou:128 ou. For subsequent higher resolution searches, we have found it sufficient to use $A:B = -2\text{BIN}:2\text{BIN}$ for all parameters.

```
Initialize variables:
R_w^best = R_φ^best = R_ψ^best = D_l^best = 0
Auto-focus search:
for BIN = 4,2,1
    S = N/BIN
    Downsample projections from N × N to S × S
    for PARM in { R_w, R_φ, R_ψ, D_l }
        Perform 1D scan over PARM
        get A : B for PARM at scale=S specified
        PARM = PARM best + A, PARM max = SHARP max = 0
        while PARM ≤ PARM best + B
            reconstruct K slices specified (keeping magnification
            fixed)
            SHARP[PARM] = sum of sharpness of each slice
            if SHARP[PARM] > SHARP max
                SHARP max = SHARP[PARM], PARM max = PARM
            end if
            PARM = PARM + BIN
        end while
        Perform parabolic fit to determine PARM best
        L = SHARP[PARM best - BIN]
        R = SHARP[PARM best + BIN]
        PARM best = PARM max + 0.5BIN(R-L)/(2SHARP max - R - L)
    end for
end for
```

[a]Author to whom correspondence should be addressed. Electronic mail: andrew.kingston@anu.edu.au

[1]A. Kingston, A. Sakallariou, A. Sheppard, T. Varslot, and S. Latham, "An auto-focus method for generating sharp 3d tomographic images", Proc. SPIE, **7804**, 78040J (2010).

[2]T. Varslot, A. Kingston, A. Sheppard, and A. Sakallariou, "Fast high-resolution micro-CT with exact reconstruction methods", Proc. SPIE, **7804**, 780413 (2010)
[3]A. Sasov, X. Liu, and P. Salmon, "Compensation of mechanical inaccuracies in micro-CT and nano-CT", Proc. SPIE,**7078**, 70781C (2008).
[4]S. Mayo, P. Miller, D. Gao, and J. Sheffield-Parker, "Software image alignment for x-ray microtomography with submicrometre resolution using a SEM-based x-ray microscope," J. Microsc. **228**, 257–263 (2007).
[5]D. Atkinson, D. Hill, P. Stoyle, P. Summers, and S. Keevil, "An autofocus algorithm for the automatic correction of motion artifacts in MR images," in *Proceedings Information. Processing in Medical Imaging* (Springer, Berlin/Heidelberg, 1997), Vol. **1230**, pp. 341–354.
[6]D. Atkinson, D. Hill, P. Stoyle, P. Summers, S. Clare, R. Bowtell, and S. Keevil, "Automatic compensation of motion artifacts in MRI," Magn. Reson. Med. **41**, 163–170 (1999).
[7]A. V. Bronnikov, "Virtual alignment of x-ray cone-beam tomography system using two calibration aperture measurements," Opt. Eng. **38**, 381–386 (1999).
[8]T. Weitkamp and P. Bleuet, "Automatic geometrical calibration for x-ray microtomography based on fourier and radon analysis," in *Proceedings of the SPIE Developments in X-Ray Tomography IV*, edited by Ulrich Bonse (2004), Vol. 5535, pp. 623–627.
[9]Y. Sun, Y. Hou, F. Zhao, and J. Hu, "A calibration method for misaligned scanner geometry in cone-beam computed tomography," NDT & E Int. **39**, 499–513 (2006).
[10]K. Yang, A. L. Kwan, D. F. Miller, and J. M. Boone, "A geometric calibration method for cone beam CT systems," Med. Phys. **33**, 1695–1706 (2006).
[11]C. Mennessier and R. Clackdoyle, "Automated geometric calibration and reconstruction in circular cone-beam tomography," in *Proceedings of the IEEE Nuclear Science Symposium*, (IEEE, Dresden, Germany, 2008), pp. 5081–5085.
[12]C. Mennessier, R. Clackdoyle, and F. Noo, "Direct determination of geometric alignment parameters for cone-beam scanners," Phys. Med. Biol. **54**, 1633–1660 (2009).
[13]I. S. Kyprianou, S. Paquerault, B. D. Gallas, A. Badano, S. Park, and K. J. Myers, "Framework for determination of geometric parameters of a cone beam CT scanner for measuring the system response function and improved object reconstruction," in *Proceedings of the IEEE International Symposium on Biomedical Imaging*, (IEEE, Arlington, VA, 2006), pp. 1248–1251.
[14]J. C. Fung, W. Liu, W. D. Ruijter, H. Chen, C. K. Abbey, J. W. Sedat, and D. A. Agard, "Toward fully automated high resolution electron tomography,"J. Struct. Biol. **116**, 181–189 (1996).
[15]D. Ress, M. L. Harlow, M. Schwarz, M. Marshall, and U. J. McMahan, "Automatic acquisition of fiducial markers and alignment of images in tilt series for electron tomography," J. Electron Microsc. **48**, 277–287 (1999).
[16]S. Brandt, J. Heikkonen, and P. Engelhardt, "Multiphase method for automatic alignment of transmission electron microscope images using markers," J. Struct. Biol. **133**, 10–22 (2001).
[17]A. Viskoe, "Computed tomography postacquisition data correction for system alignment errors," IEEE Trans. Instrum. Meas. **48**, 972–977 (1999).
[18]A. Brunetti and F. De Carlo, "A robust procedure for determination of center of rotation in tomography," in *Proceedings of the SPIE Developments in X-Ray Tomography IV*, edited by Ulrich Bonse (2004), Vol. 5535, pp. 652–659.
[19]D. Panetta, N. Belcari, A. Del Guerra, and S. Moehrs, "An optimization-based method for geometrical calibration in cone-beam CT without dedicated phantoms," Phys. Med. Biol. **53**, 3841–3861 (2008).
[20]V. Patel, R. N. Chityala, K. R. Hoffmann, C. N. Ionita, D. R. Bednarek, and S. Rudin, "Self-calibration of a cone-beam micro-CT system," Med. Phys. **36**, 48–58 (2009).
[21]Y. Kyriakou, R. M. Lapp, L. Hillebrand, D. Ertel, and W. A. Kalender, "Simultaneous misalignment correction for approximate circular cone-beam computed tomography," Phys. Med. Biol. **53**, 6267–6289 (2009).
[22]A. Sakellariou, "Investigation of misalignment errors for cone beam x-ray tomography," Internal Report (Department of Applied Mathematics Research School of Physics and Engineering, Australian National University, 2005).
[23]H. Akima, "A new method of interpolation and smooth curve fitting based on local procedures," J. Assoc. Comput. Mach. **17**, 589–602 (1970).
[24]H. Akima, "A method of bivariate interpolation and smooth surface fitting based on local procedures," Commun. ACM **17**, 18–20 (1974).
[25]T. Blu, P. Thévenaz, and M. Unser, "Linear interpolation revitalized," IEEE Trans. Image Process. **13**, 710–719 (2004).
[26]L. Feldkamp, L. Davis, and J. Kress, "Practical cone-beam algorithm," J. Opt. Soc. Am. A **1**, 612–619 (1984).
[27]B. Horn, "Focusing," Tech. Rep. Memo No. 160 (MIT Artificial Intelligence Lab., 1968).
[28]J. Kautsky, J. Flusser, B. Zitovà, and S. Šimberovà, "A new wavelet-based measure of image focus," Int. J. Pattern Recognit. Artif. Intell. **23**, 1785–1794 (2002).
[29]F. Groen, I. Young, and G. Ligthart, "A comparison of different focus functions for use in autofocus algorithms," Cytometry **6**, 81–91 (1985).
[30]J. Schlag, A. Sanderson, C. Neumann, and F. Wimberly, "Implementation of automatic focusing algorithms for a computer vision system with camera control," Tech. Rep. CMU-RI-TR-83-14 (Carnegie Mellon Univ., 1983).
[31]E. Krotkov, "Focusing," J. Comput. Vis. **1**, 223–237 (1987).
[32]M. Subbarao, T. Choi, and A. Nikzad, "Focusing techniques," J. Opt. Eng. **32**, 2824–2836 (1993).
[33]L. Shih, "Autofocus survey: a comparison of algorithms," Proc. SPIE, **6502**, 65020B (2007).
[34]T. Varslot, A. Kingston, A. Sheppard, and A. Sakellariou, "High-resolution helical cone-beam micro-tomography with theoretically-exact reconstruction from experimental data" (unpublished).
[35]A. Katsevich, "Theoretically exact filtered backprojection-type inversion algorithm for spiral CT," SIAM J. Appl. Math. **62**, 2012–2026 (2002).